Open Access

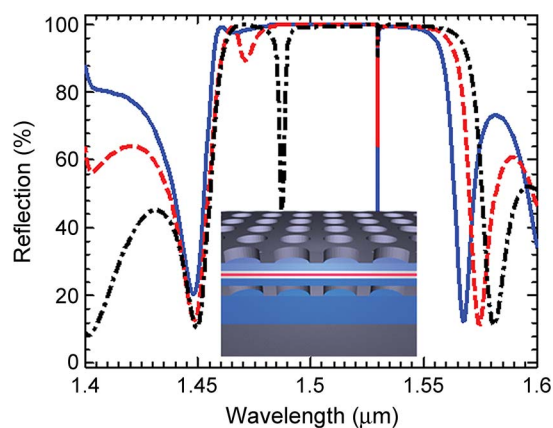# Design of Photonic Crystal Membrane-Reflector-Based VCSELs

D. Zhao
H. Yang, Member, IEEE
S. Chuwongin
J. H. Seo
Z. Ma, Member, IEEE
W. Zhou, Senior Member, IEEE

Design of Photonic Crystal Membrane-Reflector-Based VCSELs

D. Zhao,[1] **H. Yang,**[1,3] *Member, IEEE*, **S. Chuwongin,**[1] **J. H. Seo,**[2]
Z. Ma,[2] *Member, IEEE*, **and W. Zhou,**[1] *Senior Member, IEEE*

[1]Department of Electrical Engineering, NanoFAB Center, University of Texas at Arlington,
Arlington, TX 76019 USA
[2]Department of Electrical and Computer Engineering, University of Wisconsin-Madison,
Madison, WI 53706 USA
[3]Semerane, Inc., Arlington, TX 76010 USA

Abstract: We present here the cavity design of distributed-Bragg-reflector-free ultracompact Fano-resonance photonic crystal membrane-reflector vertical-cavity surface-emitting lasers on silicon, which consists of a III–V quantum-well active region sandwiched in between two single-layer Si membrane reflectors (MRs). The Si reflectors are designed to have peak reflection band around 1550 nm, with over 300-nm reflection band. The complete laser cavity resonance was determined, with considerations of unique phase and field distribution characteristics associated with these single-layer MRs. The confinement factor of the lasing mode is optimized around 6%, which enables low threshold lasing.

Index Terms: Fano resonance, photonic crystals (PCs), membrane reflectors (MRs), vertical-cavity surface-emitting lasers (VCSELs), semiconductor lasers, silicon nanophotonics.

1. Introduction

Since its first introduction [1], vertical-cavity surface-emitting lasers (VCSELs) have become a laser of choice for a wide range of applications, with low threshold, high wall plug efficiency, high modulation speed, and low-cost large-volume production [2], [3]. Traditionally, VCSELs have the optical feedback provided by the distributed Bragg reflectors (DBRs) consisting of multilayer quarter-wavelength thick dielectric layers with alternating high and low refractive indexes. Because of the very short gain lengths in VCSELs, a very high reflectivity ($> 99\%$) is required in the DBRs. Hence, the DBRs are typically very thick, consisting of many pairs of alternating index materials. While monolithically grown DBRs are mature technology for GaAs-based VCSELs, it is of great challenge for InP-based longer wavelength VCSELs, due to the lack of the lattice-matched alternative materials with large index contrast.

It is well known that single-layer 1-D grating structures and 2-D/3-D photonic crystal (PC) structures can offer very high reflectivities for certain spectral band by design. VCSELs have been reported by replacing one or two DBRs with 1-D subwavelength high contrast grating structures (SWGs or HCGs) [4], [5]. Very recently, an optically pumped VCSEL on Si was also reported based
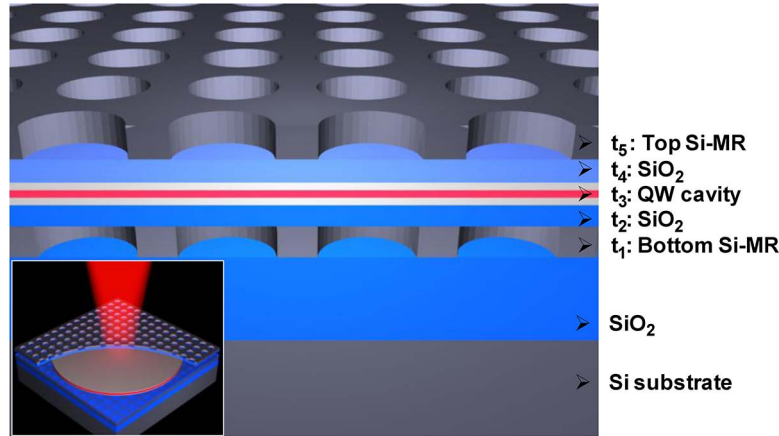
Fig. 1. (a) Schematic of MR-VCSEL lasing cavity structure, which consists of five layers $(t_1 - t_5)$: an InGaAsP QW cavity sandwiched in between two single layer Si Fano resonance PC MRs (Si-MRs), stacked on a Si substrate. Low index SiO_2 buffer layers are inserted to ensure high reflection of MRs. Inset is a complete MR-VCSEL cut-out view.

on 2-D PC Fano resonance membrane reflectors (MR) on silicon substrate, by transfer printing III–V InGaAsP quantum-well (QW) active region in between two single-layer silicon MRs [6].

Based on completely different mechanisms from DBRs, these Fano resonance PC MRs have different phase and energy penetration characteristics [7]. In this paper, we report the design procedure of these mirrors and the determination of the lasing cavity. Care was taken to identify and separate the lasing cavity mode from the waveguide mode associated with Fano resonances. With design optimization, the confinement factor for the lasing mode is ∼6%, which is similar to the values in conventional DBR-based VCSELs, despite significantly reduced effective cavity length in MR-VCSELs. Such design ensures low threshold lasing and high-performance ultracompact VCSELs on silicon and any other substrates at any wavelengths.

2. MR-VCSEL Cavity Design

As shown schematically in Fig. 1, the MR-VCSEL cavity consists of a III–V InGaAsP QW cavity (layer t_3), sandwiched in between two single-layer Si PC Fano resonance MRs (Si-MRs; layers t_1 and t_5). Two low index buffer layers (SiO_2, layers t_2 and t_4) are inserted to ensure proper index contrast to the top and bottom Si-MRs. The complete MR-VCSEL cavity (t_1 to t_5) is built on the top of a silicon-on-insulator (SOI) substrate with SiO_2 box layer thickness of t_0. In order to achieve lasing with low threshold in such a cavity, it is highly desirable to design MR-VCSEL cavity with the following characteristics: 1) Both top and bottom MRs should have broadband reflection bands, with reflections greater than 99%. 2) The cavity should be designed such that the cavity mode is spectrally separated from the waveguide modes. 3) The cavity mode should match with QW emission peak spectrally with or without spectral detuning. 4) The cavity mode should have an optimal field distribution spatially matched with the QW active region for high confinement factors and low lasing thresholds.

2.1. Si-MR Design and Optimization

A single-layer Si-MR with 1-D or 2-D PC pattern can be functioned as broadband reflectors. Based on the previous reports [8]–[11], we choose Si-MR thickness (t_1 and t_5 shown in Fig. 1) of 340 nm (with Si index $n = 3.48$) to design MRs with high broadband spectral reflection in the optical communication band around 1550 nm. In our current design, we mainly focus on the square lattice air hole PC structure, with air hole radius r and lattice constant a. The design is based on rigorous coupled-wave analysis (RCWA) [12] technique and 3-D finite-difference time domain (FDTD) method [13]. A set of optimized designs for both top and bottom Si-MRs are shown in Fig. 2(a) and
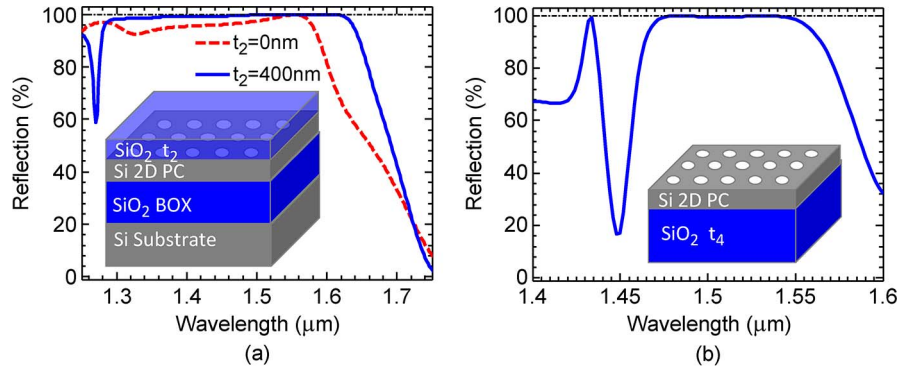
Fig. 2. Simulated reflection spectra for top and bottom Si-MRs: (a) Bottom Si-MR based on SOI structure with SiO$_2$ deposition on top as the low index buffer layer with thickness $t_2 = 0$ nm and 400 nm, respectively; (b) Top Si-MR another low index SiO$_2$ buffer layer with thickness $t_4 = 400$ nm. Shown in the insets are the schematics of bottom and top Si-MR structures.

(b), respectively. It is worth noting that, for the bottom Si-MR, in addition to the bottom Si substrate and SiO$_2$ BOX layer (t_0) right below the Si-MR layer, another layer of SiO$_2$ low index buffer layer (t_2) is also incorporated in the design, as part of the complete MR-VCSEL as shown in Fig. 1. During the deposition of top SiO$_2$ layer (t_2), there will be partial deposition of SiO$_2$ inside the air holes of Si-MR region, which results in an increased effective index inside the air hole region (n_f). Based on earlier theoretical and experiment results [9], the effective index for the air hole region (n_f) is about 1.2 for Si-MRs with larger air hole design ($r/a > 0.4$). For the design shown in Fig. 2(a) for bottom Si-MR, the design parameters are $t_0 = 1$ μm, $t_1 = 340$ nm, $a = 880$ nm, $r/a = 0.45$, $n_f = 1.2$, and $t_2 = 0$ nm and 400 nm, respectively. One can see that the reflection band for $t_2 = 400$ nm covers from 1300 to 1600 nm with reflection $R > 99\%$. The top Si-MR, on the other hand, consists of Si-NM layer with air and SiO$_2$ low index buffer layer (t_4) on the top and bottom, respectively, as shown in the inset in Fig. 2(b). The design parameters for top Si-MR design shown in Fig. 2(b) are $t_5 = 340$ nm, $a = 1010$ nm, $r/a = 0.3$, $n_f = 1.0$, and $t_4 = 400$ nm. Notice that, since there is no SiO$_2$ deposition inside the air hole region of top Si-MR, the effective index for top Si-MR air hole is 1.0. Through adjusting three main parameters (t, a, and r), we can obtain MRs for different band range. More examples or reflection parameter map can be also found in [9].

2.2. Waveguide Mode of the Active Layer

In our MR-VCSEL structure, the center InGaAsP QW cavity layer (thickness t_3) design is based on the one used in previously reported DBR-based 1550-nm VCSEL structures [6], which consists of eight InGaAsP QW layers, InGaAsP spacer layers, cladding layers, and top and bottom contact layers. The total thickness for the InGaAsP QW cavity is $t_3 = 465$ nm. In our simulation, the index and thicknesses of each layer in the center InGaAsP QW cavity layer are listed in Table 1.

The complete MR-VCSEL design mainly focuses on the optimization of top and bottom low index buffer layer thicknesses (t_2 and t_4) for optimized spectral location (cavity mode) and spatial overlap (confinement factor). One of the interesting features associated with complete MR-VCSEL design is the coexistence of both the lasing cavity mode and the waveguide mode. The designs for complete MR-VCSEL cavities are shown in Fig. 3(a), with different buffer layer (t_2 and t_4) thicknesses (thus different total cavity lengths). Here, the same lattice constant parameter is used for both top and bottom Si-MRs with $a = 945$ nm. The air hole sizes for the top and bottom Si-MRs (r/a) are 0.26 and 0.28, respectively. For smaller r/a values, a smaller effective index for the air hole region is used, with $n_f = 1.1$. The thicknesses for the low index oxide buffer layers ($t_2 = t_4$) vary from 400 to 480 nm. Lasing cavity mode shifts with the change of the total cavity length. On the other hand, the waveguide mode [around 1529 nm shown in Fig. 3(a)], which is associated with the coupling of Si-MRs with QW active layer, does not shift with the change of the MR-VCSEL cavity length. During the laser cavity design, it is best to design the cavity with this waveguide mode decoupled from the

TABLE 1

InGaAsP QW structure used in simulation

| Layer	Description	Material	Thickness (nm)	Optical Index
9	Contact layer	InGaAs	40	3.444
8	Cladding layer	InP	50	3.172
7	Spacer layer	InP	81.5	3.172
6	Quantum wells	$In_{0.485}Ga_{0.515}As_{0.83}P_{0.17}$	33.75	3.4
5	Quantum wells	$In_{0.76}Ga_{0.24}As_{0.83}P_{0.17}$	60	3.5
4	Quantum wells	$In_{0.485}Ga_{0.515}As_{0.83}P_{0.17}$	33.75	3.4
3	Spacer layer	InP	81.5	3.172
2	Cladding layer	InP	50	3.172
1	Contact layer	InGaAs	40	3.444
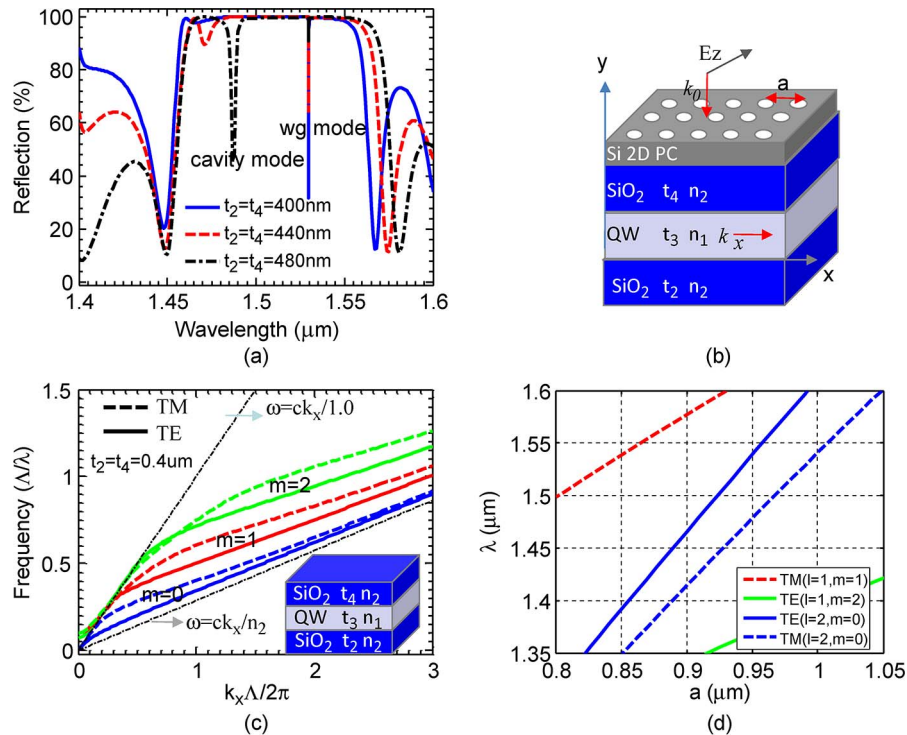
Fig. 3. Waveguide mode inside MR-VCSEL cavity: (a) Reflections of MR-VCSEL cavity with different buffer layer thickness. (b) Schematic of a plane waveguide with a grating on top. (c), Dispersion of the plane waveguide, where top and bottom are covered with 400 nm SiO_2 and $\Lambda = 1 \ \mu m$. (d) Possible waveguide modes excited by top grating through coupling at different grating period.

cavity mode to avoid any loss associated with this waveguide. The waveguide mode can be analyzed based on traditional waveguide theory on the simplified structure shown in Fig. 3(b) [14].

The high index waveguide layer (t_3, n_1), shown in Fig. 3(b), consists of the InGaAsP QW cavity, with thickness $t_3 = 465$ nm and effective index $n_1 = 3.34$. Two low index buffer layers represent the low index oxide buffer layers (t_2 and t_4 in Fig. 1), with $n_2 = 1.45$. The dispersion characteristics for the QW layer planar waveguide with two buffer layers can be obtained by solving the traditional waveguide equations [14] or using 2-D model of plane wave expansion method [15]. Fig. 3(c)
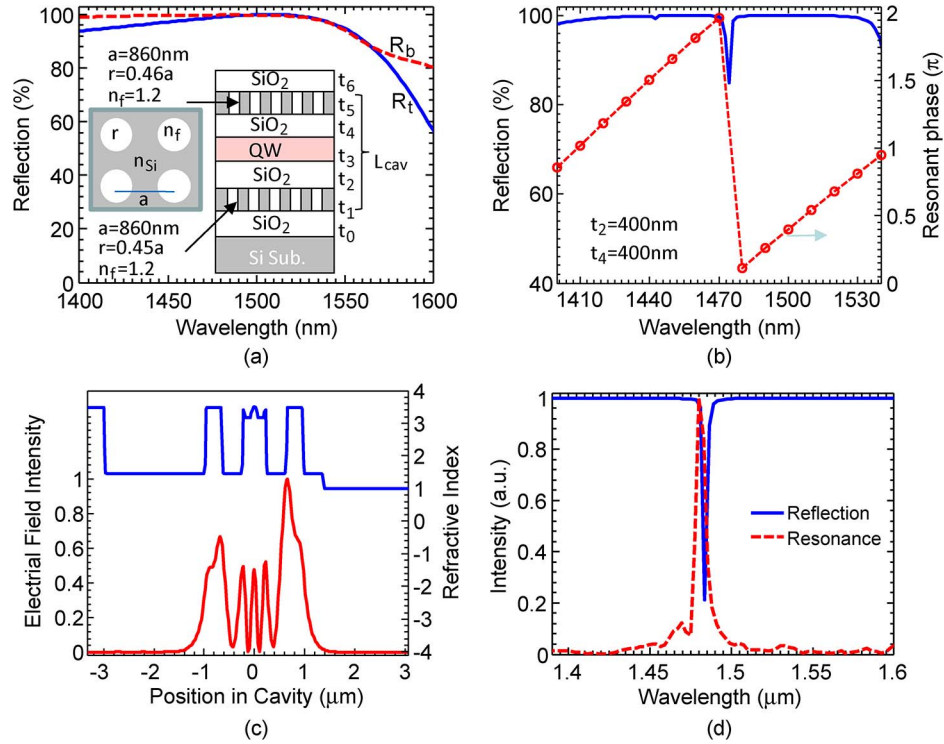
Fig. 4. Characteristics of designed MR-VCSEL cavity: (a) Reflections of top and bottom MRs, inset is the MR-VCSEL cavity structure configuration, where $t_0 = 2$ μm, $t_1 = t_5 = 340$ nm, $t_2 = t_4 = 400$ nm, $t_6 = 400$ nm. (b) Calculated cavity resonance mode based on cavity reflection and phase resonant condition. (c) Field distribution of cavity mode. (d) Cavity mode of MR-VCSEL cavity with finite size. Reflections (blue lines) and resonant (red dash lines) spectra of MR-VCSEL for Low T at $\lambda = 1478$ nm.

shows the lowest three orders $(m = 0, 1, 2)$ of the QW waveguide for TE and TM modes, respectively. Due to the presence of the 2-D grating (PC) on the top, some of the waveguide modes can be excited through the coupling between the 2-D grating and the planar waveguide. The excited waveguide mode depends on the grating period a in both orthogonal directions. For the normal incidence, the coupling condition can be written into [16]

$$|k_{x,m}| = |k_{y,m}| = l\frac{2\pi}{a}, \qquad l = 1, 2, \ldots \tag{1}$$

where l is the grating diffraction order. According to (1), we can find the correlation between the excited waveguide mode (wavelength λ) and the coupling grating period a. The result is plotted in Fig. 3(d) for the wavelength range from 1350 nm to 1600 nm with grating period range from 800 nm to 1050 nm. One can find that, when $a = 945$ nm, a waveguide mode is located near 1529 nm. When $a = 860$ nm or 880 nm, there is no waveguide mode in the wavelength range from 1420 to 1550 nm, and when $a = 980$ nm, there is also no waveguide mode near 1550 nm. Therefore, to avoid the possible waveguide mode or to ensure these waveguide modes are spectrally located far away from the expected cavity mode, special care should be paid on the choice of the Si-MR PC lattice constants.

2.3. MR-VCSEL Cavity Mode

Taking into considerations the above analysis, Si-MRs were designed with lattice constant of $a = 860$ nm. An example of a complete MR-VCSEL cavity design is shown in Fig. 4. As shown schematically in the inset of this complete MR-VCSEL, relatively large air hole radius is used here for the Si-MRs, with $r/a = 0.46$ and 0.45 for the top and bottom Si-MRs, respectively. Other parameters are optimized to be $t_0 = 2$ μm, $t_1 = t_5 = 340$ nm, and $t_3 = 465$ nm, respectively. Now,

only the thicknesses of the low index buffer layers (t_2 and t_4) can be tuned to adjust the cavity mode location. To make the field distribution more symmetric inside cavity, another SiO_2 layer with $t_6 = 400$ nm or thicker is assumed to be deposited on the top of MR-VCSEL, and $n_f = 1.2$ is also considered for the top Si-MR, which has similar low index material surrounding as bottom Si-MR. In simulation, a periodical boundary condition is used, i.e., the lateral dimension is infinite. Fig. 4(a) demonstrates the simulated reflections for the top and bottom Si-MRs based on 3-D FDTD, with peak reflection of 100% and high reflection band ($> 98\%$) covering the wavelength range from 1420 to 1530 nm.

We use two different techniques to decide the cavity mode through tuning the two buffer layer thicknesses. The first one is to calculate the reflection of the whole cavity structure. From the dips located into the high reflection band range, we can easily find the cavity mode according to its resonant transmission property. The reflection of MR-VCSEL with $t_2 = t_4 = 400$ nm is plotted in Fig. 4(b) with the blue line, which is calculated with RCWA technique. We can find that the dip is located at 1478 nm. To confirm this cavity mode, a method based on phase resonant condition (total phase change of one roundtrip in cavity is equal to the integer times of 2π) is used to decide the cavity mode. The phase calculation details can be found in [7]. After obtaining the reflection phase change (ϕ) of the top and bottom Si-MRs, the resonant cavity mode can be easily decided. The phase of the mode in cavity is shown in Fig. 4(b) with red dash-dotted line, which is plotted in the range of $[0, 2\pi]$. One can find the mode located at 1478 nm with a 2π phase shift, which confirms that 1478 nm is a real cavity mode.

The quality factor and the field distribution of this cavity mode are investigated. By employing FDTD technique, a short temporal Gaussian pulse is used to excite the cavity mode, and the quality factor of the cavity mode at 1478 nm is calculated to be 4300 according to $Q = \mathrm{Re}(\omega)/-2\mathrm{Im}(\omega)$. Then, a longer temporal Gaussian pulse is used to excite only this cavity mode, and the stable field is recorded after the source is turned off for a long time. The E-field of the standing-wave distribution is demonstrated in Fig. 4(c) with a red line, where the cavity index profile is also plotted with a blue line. One can see that one of the E-field peaks is located at QW region, and we calculated that the confinement factor is about $\Gamma = 5.6\%$ according to $\int_{QW} E^2 dv / \int_{cav} E^2 dv$. It is worthy to note that the field intensity inside the top and bottom Si-MRs is also relatively large. This is because of the Fano resonance reflection mechanism, i.e., guided mode excitation in Si-MRs [7], [17]. Although the field intensity inside Si-MR is large, it does not give rise to much cavity loss and the absorption loss since Si itself is transparent around 1550 nm. Most importantly, owing to the strong confinement in the much reduced cavity lengths, the calculated confinement factor for Si-MR is similar to the typical confinement factors obtained in conventional DBR-based VCSELs. This critical feature enables low threshold lasing in the MR-VCSEL cavities.

Finally, for the practical MR-VCSEL design, the top and bottom Si-MRs may have different PC lattice parameters. Additionally, the cavity has a finite size. In this case, instead of the simple periodical boundary condition, the perfect-match layer (PML) boundary condition is used in FDTD simulations. Here, we studied the cavity configurations with a square size $\sim 22 \times 22$ μm^2, $a_t = 860$ nm, $r_t = 0.46a_t$, $a_b = 880$ nm, $r_b = 0.45a_b$, $t_2 = 380$ nm, and $t_4 = 420$ nm. The reflection of the cavity is obtained by calculating the reflected flux outside the cavity, and the resonant mode is found through the Fourier transfer of $E(t)$ of one monitor inside the cavity. The reflection and resonant spectra are plotted together with blue solid and red dashed lines, as shown in Fig. 4(d). One can find that the cavity mode matches well between the dip in the reflection spectrum and the peak in the resonant spectrum. In addition, the estimated Q of this cavity mode is ~ 1100, which is largely limited by the relatively short time steps in FDTD simulation. The simulation time and structure size are limited by the memory and the CPU number. Much higher cavity Q is expected considering real structures with large sizes and better simulation resolutions.

3. Conclusion

In conclusion, we have reported here the design of a new type of MR-VCSEL on Si. The design of the single-layer Fano resonance top and bottom Si-MRs has been discussed by considering the

reflection amplitude and phase delays, as well as the impact of the potential waveguide mode. Due to drastically different phase differences and different reflection mechanisms, the cavity resonance modes, along with the field distribution profiles, are quite different from the lasing cavities formed with two conventional DBRs. Despite the relatively large field concentration in the high index Si-MR layers, the lasing mode field confinement factor is ∼5.6% for MR-VCSELs, which is comparable with DBR-based VCSELs. Such high confinement factor may be a result of the much reduced lasing cavity length and stronger cavity confinement, due to the reduced field penetration depths. This feature ensures such kind of ultracompact MR-VCSELs to have performance similar or better than conventional DBR-based VCSELs, with reduced threshold and improved energy efficiency, highly desirable for on-chip photonic and electronic integration [6].

Acknowledgment

References

[1] K. Iga, F. Koyama, and S. Kinoshita, "Surface emitting semiconductor-lasers," *IEEE J. Quantum Electron.*, vol. QE-24, no. 9, pp. 1845–1855, Sep. 1988.

[2] K. Iga, "Surface-emitting laser—Its birth and generation of new optoelectronics field," *IEEE J. Sel. Topics Quantum Electron.*, vol. 6, no. 6, pp. 1201–1215, Nov./Dec. 2000.

[3] C. W. Wilmsen, H. Temkin, and L. A. Coldren, *Vertical-Cavity Surface-Emitting Lasers: Design, Fabrication, Characterization, and Applications*.   Cambridge, U.K.: Cambridge Univ. Press, 2001.

[4] M. C. Y. Huang, Y. Zhou, and C. J. Chang-Hasnain, "A surface-emitting laser incorporating a high-index-contrast subwavelength grating," *Nat. Photon.*, vol. 1, no. 5, pp. 297–297, May 2007.

[5] C. Sciancalepore, B. B. Bakir, X. Letartre, J. Harduin, N. Olivier, C. Seassal, J. Fedeli, and P. Viktorovitch, "CMOS-compatible ultra-compact 1.55-μm emitting VCSELs using double photonic crystal mirrors," *IEEE Photon. Technol. Lett.*, vol. 24, no. 6, pp. 455–457, Mar. 15, 2012.

[6] H. Yang, D. Zhao, S. Chuwongin, J. H. Seo, W. Yang, Y. Shuai, J. Berggren, M. Hammar, Z. Ma, and W. Zhou, "Transfer-printed stacked nanomembrane lasers on silicon," *Nat. Photon.*, vol. 6, no. 6, pp. 617–622, Sep. 2012.

[7] D. Y. Zhao, Z. Q. Ma, and W. D. Zhou, "Field penetrations in photonic crystal Fano reflectors," *Opt. Exp.*, vol. 18, no. 13, pp. 14 152–14 158, Jun. 21, 2010.

[8] H. J. Yang, S. Chuwongin, Z. X. Qiang, L. Chen, H. Q. Pang, Z. Q. Ma, and W. D. Zhou, "Resonance control of membrane reflectors with effective index engineering," *Appl. Phys. Lett.*, vol. 95, no. 2, pp. 023110-1–023110-3, Jul. 13, 2009.

[9] Z. X. Qiang, H. J. Yang, S. Chuwongin, D. Y. Zhao, Z. Q. Ma, and W. D. Zhou, "Design of Fano broadband reflectors on SOI," *IEEE Photon. Technol. Lett.*, vol. 22, no. 15, pp. 1108–1110, Aug. 1, 2010.

[10] H. J. Yang, D. Y. Zhao, J. H. Seo, S. Chuwongin, S. Kim, J. A. Rogers, Z. Q. Ma, and W. D. Zhou, "Broadband membrane reflectors on glass," *IEEE Photon. Technol. Lett.*, vol. 24, no. 6, pp. 476–478, Mar. 15, 2012.

[11] V. Lousse, W. Suh, O. Kilic, S. Kim, O. Solgaard, and S. H. Fan, "Angular and polarization properties of a photonic crystal slab mirror," *Opt. Exp.*, vol. 12, no. 8, pp. 1575–1582, Apr. 19, 2004.

[12] E. P. Michel Neviere, *Light Propagation in Periodic Media: Differential Theory and Design*.   New York: Marcel Dekker, 2003.

[13] A. F. Oskooi, D. Roundy, M. Ibanescu, P. Bermel, J. Joannopoulos, and S. G. Johnson, "MEEP: A flexible free-software package for electromagnetic simulations by the FDTD method," *Comput. Phys. Commun.*, vol. 181, no. 3, pp. 687–702, 2010.

[14] B. E. A. Saleh, M. C. Teich, and B. E. Saleh, *Fundamentals of Photonics*.   Hoboken, NJ: Wiley, 1991.

[15] S. G. Johnson and J. D. Joannopoulos, "Block-iterative frequency-domain methods for Maxwell's equations in a planewave basis," *Opt. Exp.*, vol. 8, no. 3, pp. 173–190, Jan. 2001.

[16] Y. C. Wang and S. S. Li, "Design of a two-dimensional square mesh metal grating coupler for a miniband transport GaAs quantum-well infrared photodetector," *J. Appl. Phys.*, vol. 75, no. 1, pp. 582–587, Jan. 1994.

[17] R. Magnusson and M. Shokooh-Saremi, "Physical basis for wideband resonant reflectors," *Opt. Exp.*, vol. 16, no. 5, pp. 3456–3462, Mar. 2008.